Supplementary Information

Bifunctional PVDF/MXene Membranes with High Piezoelectric Sensitivity and Near-Infrared Photothermal Antibacterial Efficacy toward Wearable Human Activity Monitoring

Zilu Hu [a, #], Fuhao Wu [a, #], Hongbin Su [a], Wenwu Wang [a], Liang He [a, f, *], Yihao Long [a], Zeyu Ma [a], Manjia Wu [a], Yixin Wang [d], Rongwei Xu [a], Leixin Wu [a], Arif Ullah Khan [a], Huimin Liang [a], Yibo Xiong [a], Xiyao Huang [a], Yixiao Dong [e], Hongbo Yin [c*], Dan Lu [b*]

a. School of Mechanical Engineering, State Key Laboratory of Intelligent Construction and Healthy Operation and Maintenance of Deep Underground Engineering, Sichuan University, Chengdu 610065, P. R. China

b. Department of Otorhinolaryngology, Head & Neck Surgery, West China Hospital, Sichuan University, Chengdu 610041, P. R. China

c. Department of Ophthalmology, West China Hospital, Sichuan University, Chengdu 610041, P. R. China

d. School of Mechatronical Engineering, Beijing Institute of Technology, Beijing 100081, P. R. China

e. Pritzker School of Molecular Engineering, The University of Chicago, Chicago, IL 60637, USA

f. Med+X Center for Manufacturing, West China Hospital, Sichuan University, Chengdu 610041, P. R. China

* Correspondence: danlv2008@wchscu.cn (D. Lu); hongbo_yin@163.com (H. B. Yin); hel20@scu.edu.cn (L. He)

Fig. S1 shows the optical images of the obtained PVDF/MXene membrane. As can be observed from the figures, the flexibility of the film is excellent.

Fig. S1. Digital photographs of electrospun PVDF/MXene membrane.

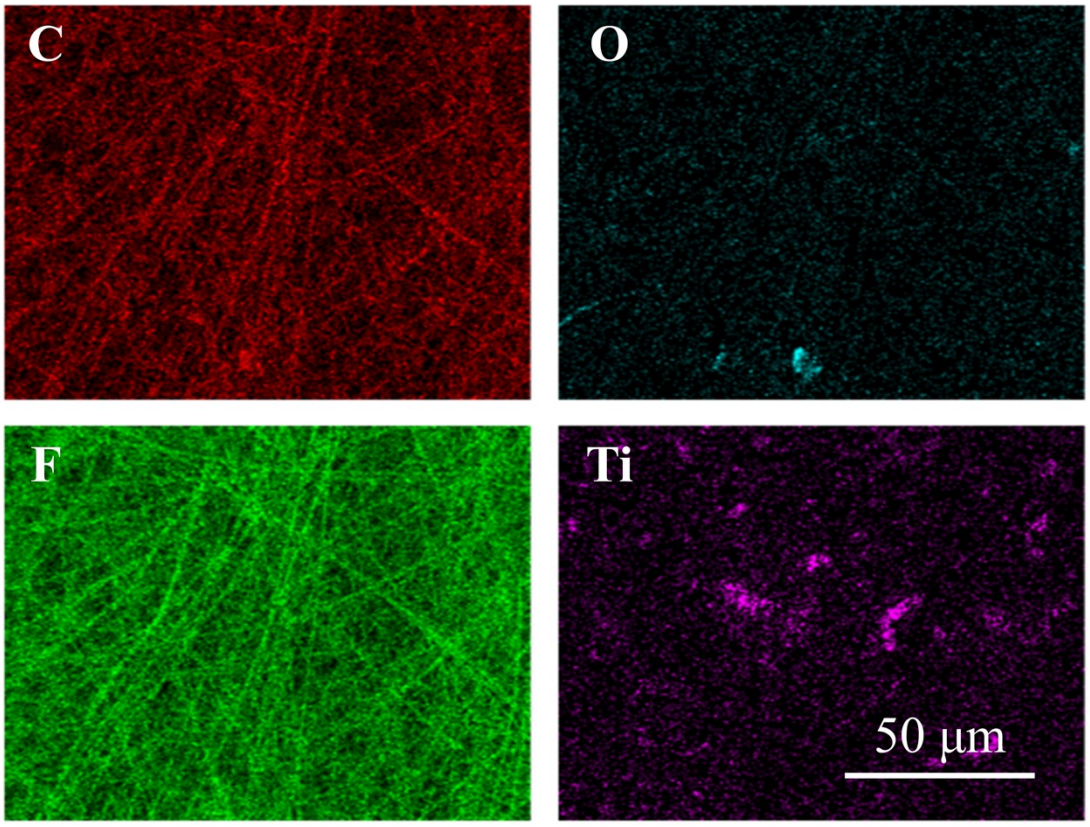

Fig. S2. Energy dispersive spectrometer (EDS) mapping images of PVDF/MXene membrane.

During the electrospinning process, the morphology of the fibers is influenced by various factors, including the concentration of the spinning solution, applied voltage, and feeding rate. To obtain the optimal electrospinning process parameters, this study employed a single-factor variable control method, for which the concentration of the PVDF solution, applied voltage, and the concentration of MXene were individually adjusted. The specific settings and experimental configurations for these three parameters are provided in Table S1.

For other electrospinning parameters, their impacts on the morphology of the nanofibers are relatively minor, so appropriate values were selected and controlled in the experiment. In this study, the feeding rate was set at 0.02 mL/min, the collection distance was 15 cm, and the rotating speed of the collection drum was set at 500 rpm.

Table S1. Electrospinning parameters in this work.

Parameters	Values
Electrospinning voltage (kV)	14, 16, 18, 20, and 22
PVDF concentration (wt.%)	10, 12, 14, 16, and 18
MXene concentration (mg/mL)	0, 1, 3, and 5

By controlling a single variable, the optimal PVDF concentration, spinning voltage, and MXene concentration were obtained, and the optimized experimental parameters were summarized.

As shown in Fig. S3(a), when the solution concentration is 10 wt.%, the resulting fiber membrane exhibits poor surface morphology, with uneven fiber distribution and significant presence of bead-like structures that have not been fully stretched. As the concentration increases to 14 wt.% and above, the solution's viscosity increases significantly, leading to enhanced molecular chain entanglement, which effectively suppresses the formation of bead structures. This results in PVDF membranes with a more uniform distribution of fiber diameter, a continuous surface, and the absence of bead-like structures.

As shown in Fig. S3(b), under the same PVDF concentration, the SEM images indicate that uniform nanofibers can be formed when the electrospinning voltage is between 14 kV and 22 kV. Previous studies indicated that, compared with the spinning solution concentration, the electrospinning voltage has a relatively small impact on the piezoelectric performance of the fibers.[1] Low voltage will fail to generate a stable jet, resulting in discontinuous fibers, while high voltage will pose safety risks to the equipment. Considering both fiber formation stability and experimental safety, 18 kV is selected as the optimal electrospinning voltage in this study.

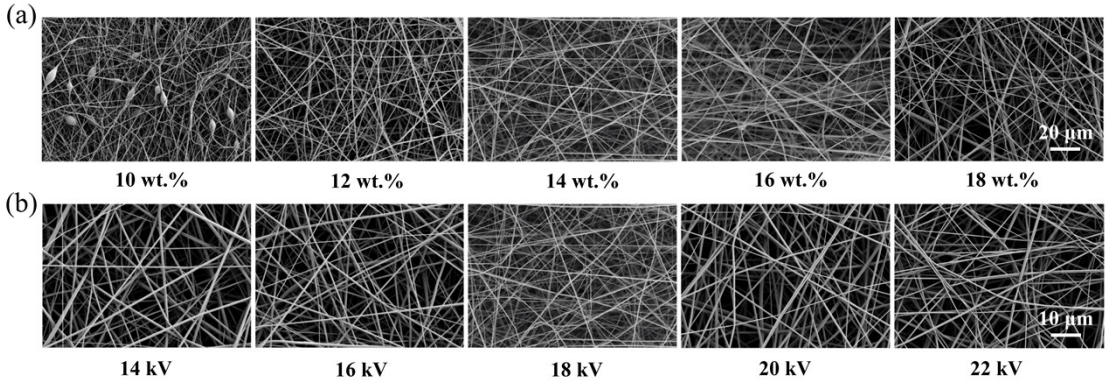

Fig. S3. (a) SEM images of PVDF nanofiber membranes with different concentrations. (b) SEM images of PVDF nanofiber membranes synthesized under different electrospinning voltages.

The fiber diameter distribution at different concentrations was obtained using the image processing software Image-J through statistically analyzing the fiber diameters of nanofiber membranes with different PVDF concentrations, as shown in Fig. S2. It can be observed that the diameter of the nanofibers increases as the PVDF concentration increases.

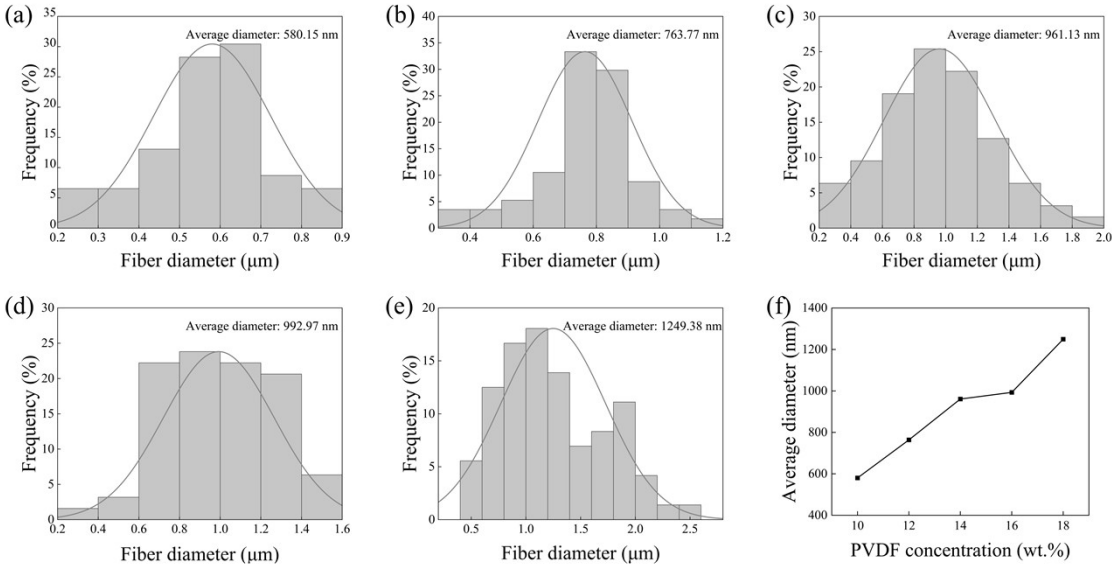

Fig. S4. Diameter distribution of PVDF nanofiber membranes with different concentrations: (a) 10 wt.%, (b) 12 wt.%, (c) 14 wt.%, (d) 16 wt.%, and (e) 18 wt.%. (f) Relationship of average diameter and PVDF concentration.

Fig. S3 shows the fiber diameter distribution diagrams under each electrospinning voltage. It can be observed that the diameter of the nanofibers decreases as the electrospinning voltage increases.

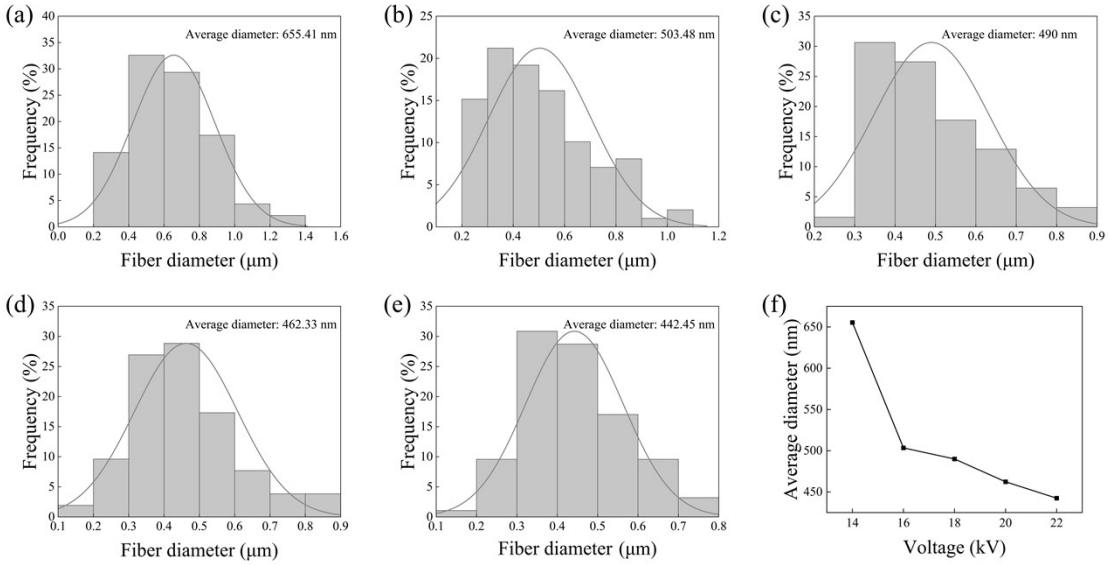

Fig. S5. Diameter distribution of PVDF nanofibers under different spinning voltages: (a) 14 kV, (b) 16 kV, (c) 18 kV, (d) 20 kV, and (e) 22 kV. (f) Relationship between average diameter and spinning voltage.

Fig. S4 shows the fiber diameter distribution under different concentrations of MXene. It can be observed that as the MXene content increases, the fiber diameter decreases. This is because the incorporation of MXene enhances the solution's electrical conductivity, thereby increasing the electric-field force on the PVDF fibers.

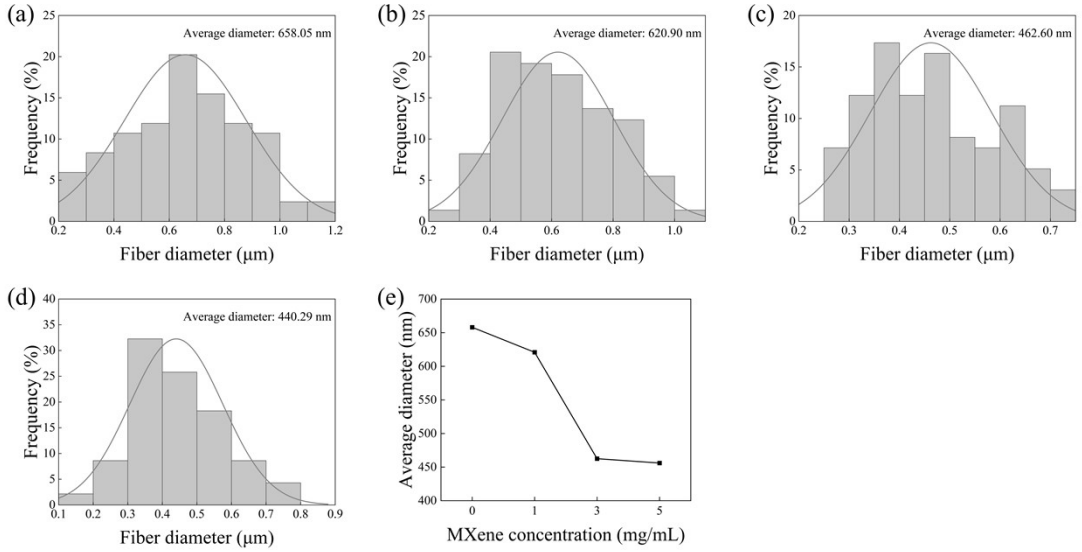

Fig. S6. Distribution of PVDF nanofiber diameters at different concentrations of MXene: (a) 0 mg/mL, (b) 1 mg/mL, (c) 3 mg/mL, and (d) 5 mg/mL. (e) A curve showing the relationship between MXene concentration and average diameter.

The results indicate that the piezoelectric coefficient reaches its maximum value when the PVDF concentration is 14 wt.%. As shown in Fig. S2, when the PVDF concentration is greater than or equal to 14 wt.%, the resulting fibers exhibit a uniform distribution and intact structure. Therefore, considering both fiber morphology and piezoelectric performance, the optimal concentration of PVDF is determined to be 14 wt.%.

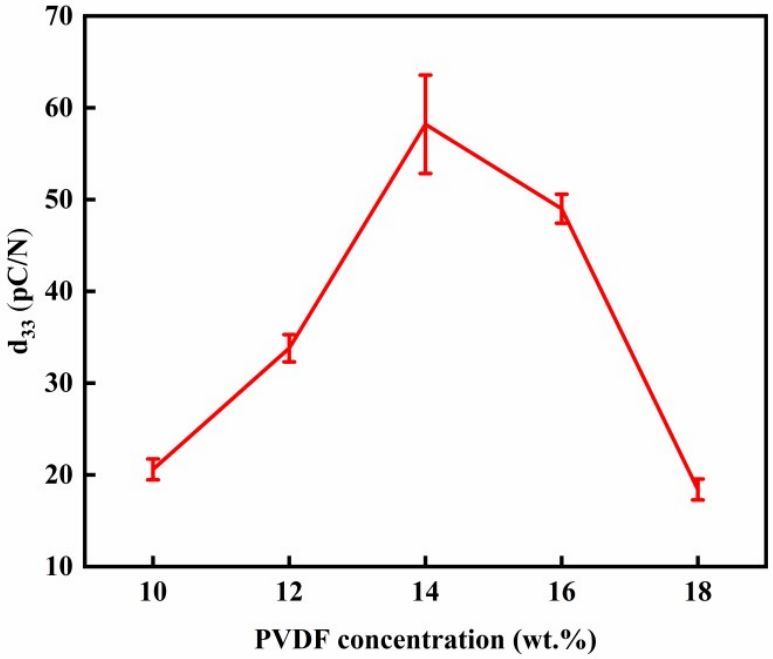

Fig. S7. d_{33} values of PVDF membranes with different concentrations.

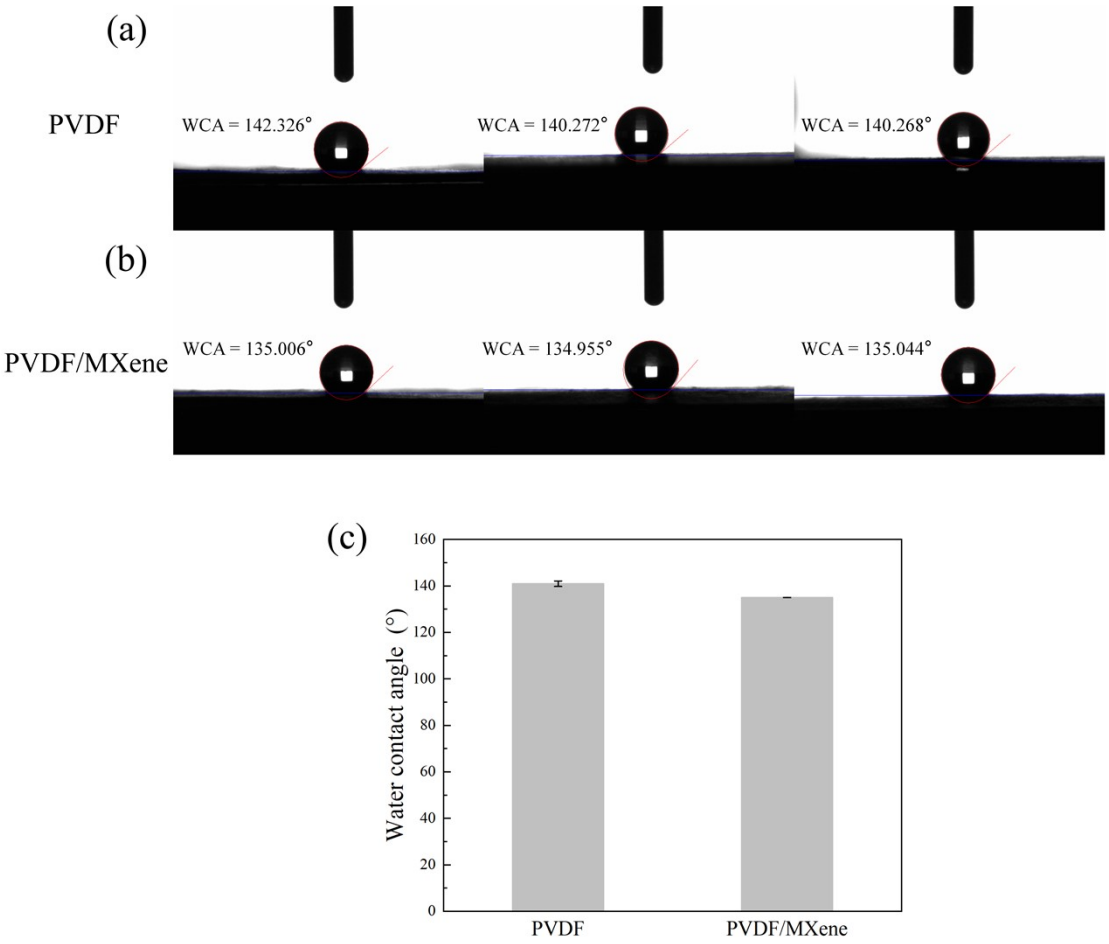

Fig. S8. Surface wettability characterization results. (a-b) Representative water contact angle (WCA) images of PVDF and PVDF/MXene composite membranes. (c) Statistical analysis of WCA values (n = 3).

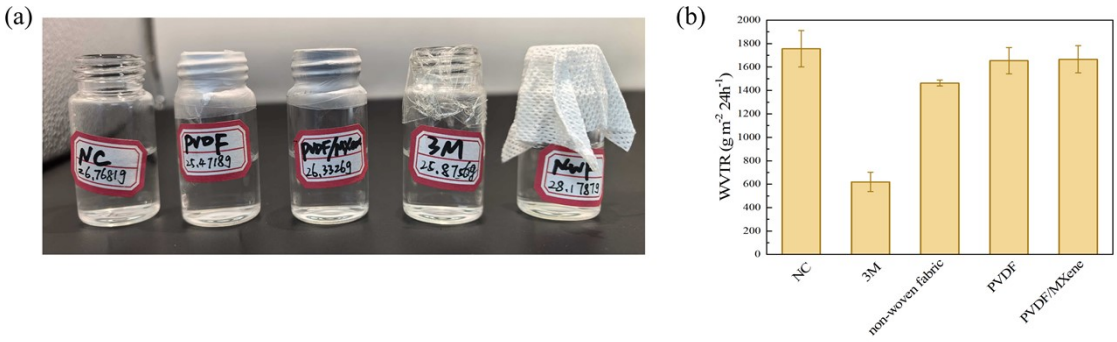

Fig. S9. (a) Schematic diagram of the WVTR measurement of different samples. (b) The WVTR of the different membranes. All the data are shown as mean ± SD (standard deviation), n = 3.

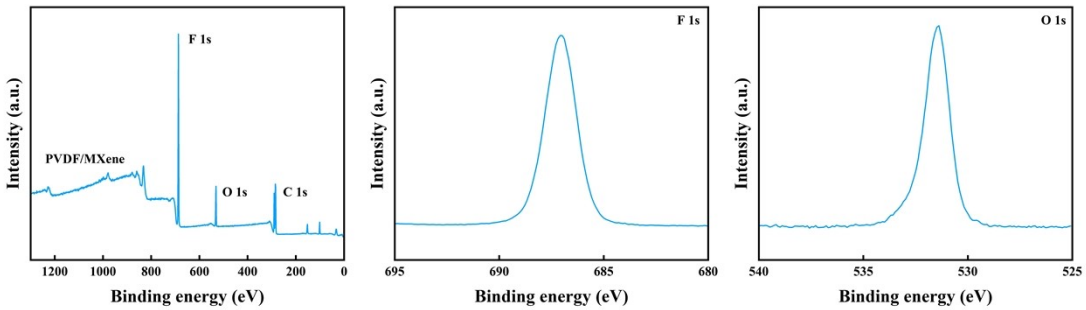

Fig. S10. XPS spectra of PVDF/MXene membrane. (a) The full XPS spectrum of the PVDF/MXene membrane. (b) F 1s region XPS spectrum of PVDF/MXene membrane. (c) O 1s region XPS spectrum of PVDF/MXene membrane.

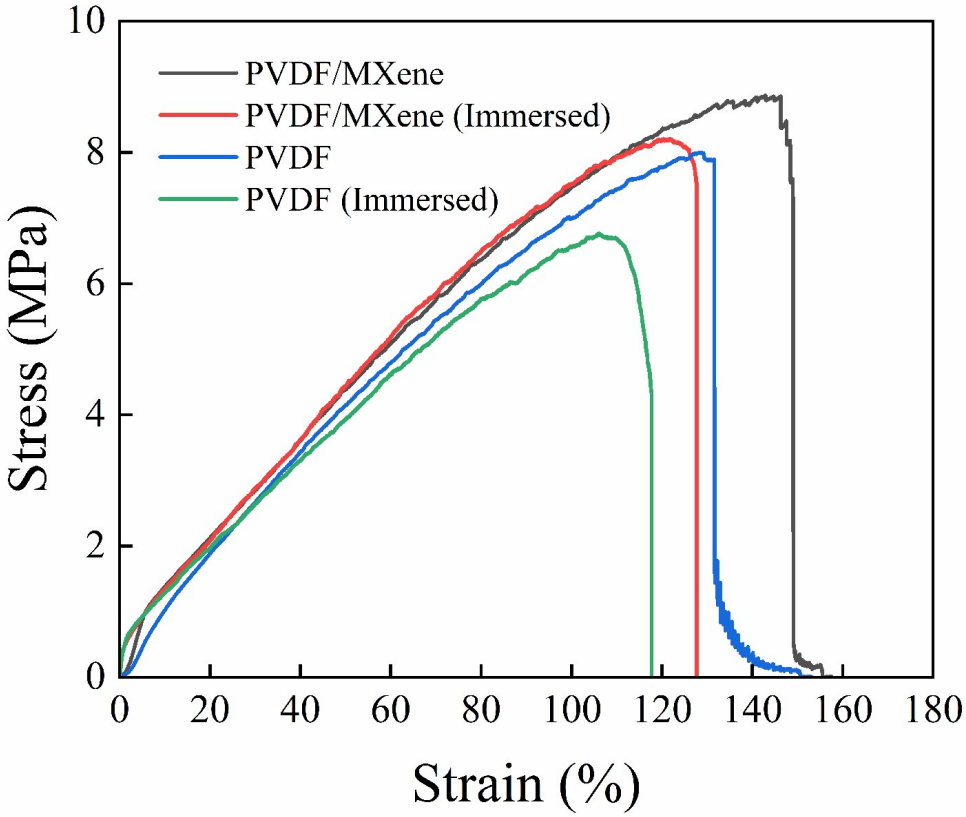

Fig. S11. Mechanical stability assessment in a simulated physiological environment. Representative tensile stress-strain curves of the PVDF membrane and the PVDF/MXene composite membrane (3 mg/mL) before and after immersion in phosphate-buffered saline (PBS, pH = 7.4) for 24 h.

Figure S10 illustrates the schematic of the entire electronic circuit. Charge amplification, filtering, and other measurement and control circuits are employed to amplify the piezoelectric signals of the film and perform noise reduction. The STM32 microcontroller is responsible for executing analog-to-digital conversion (ADC) and facilitating real-time data transmission to the host computer.

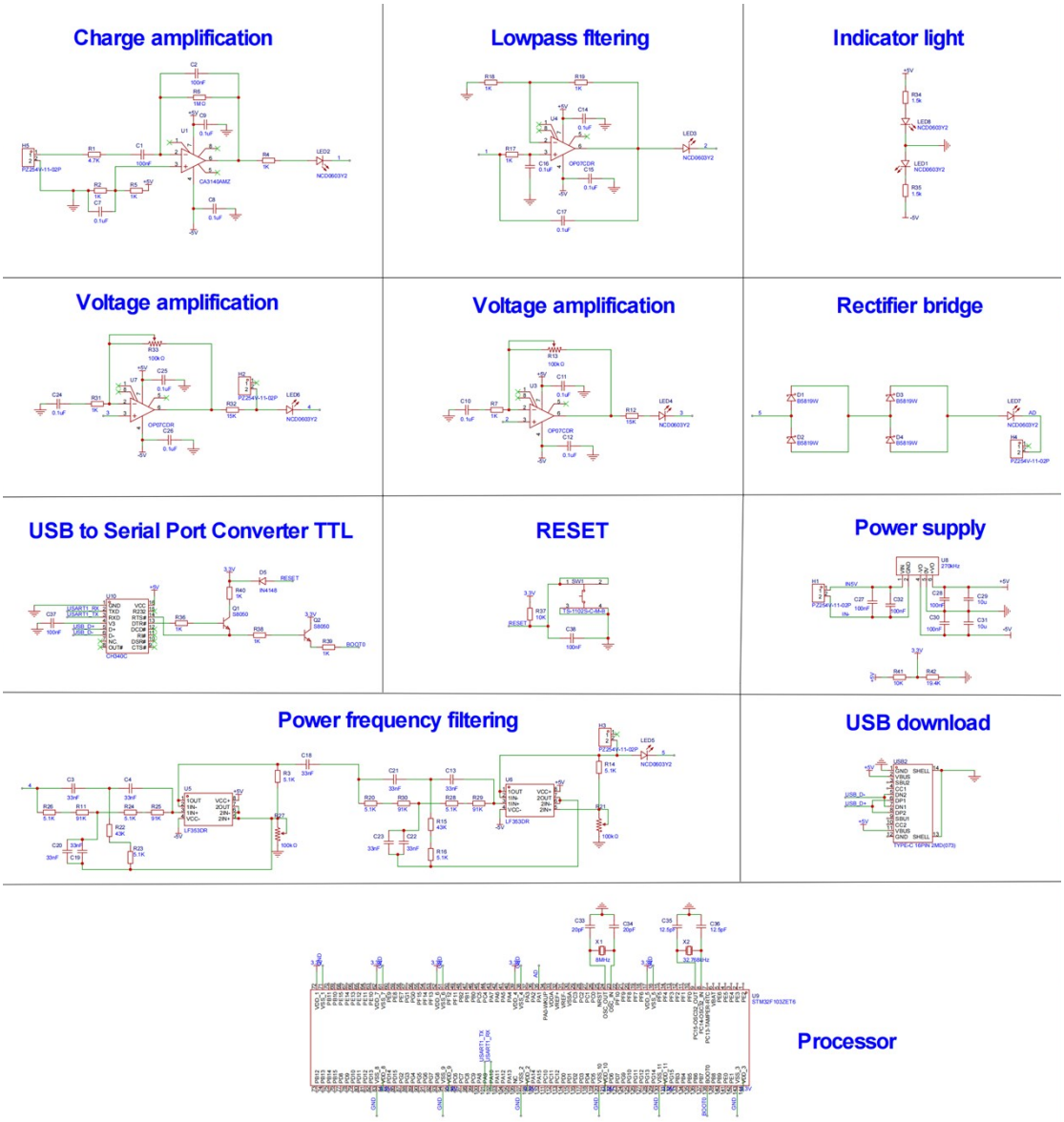

Fig. S12. Schematic of the electronic circuit, including charge amplification, filtering, and ADC conversion by the STM32 microcontroller for real-time data transmission to the host computer.

The integration of PVDF/MXene composites with electronic circuits demonstrates substantial potential in applications across various physiological motion monitoring fields. As depicted in Figure S11 (a), we successfully established a precise correlation between the piezoelectric film waveforms and real-time sampling data through the electronic circuitry. The piezoelectric film accurately senses the pressure at the sole of the foot, while the electronic circuit system transmits this data in real time to the host computer. To ensure the measurement's accuracy, an oscilloscope is employed to monitor the output waveform of the circuit system, thereby validating the reliability of the measured results. Figure S11 (b) presents the physical PCBs of the STM32 (i), the filtering circuit (ii), and the charge amplification circuit (iii).

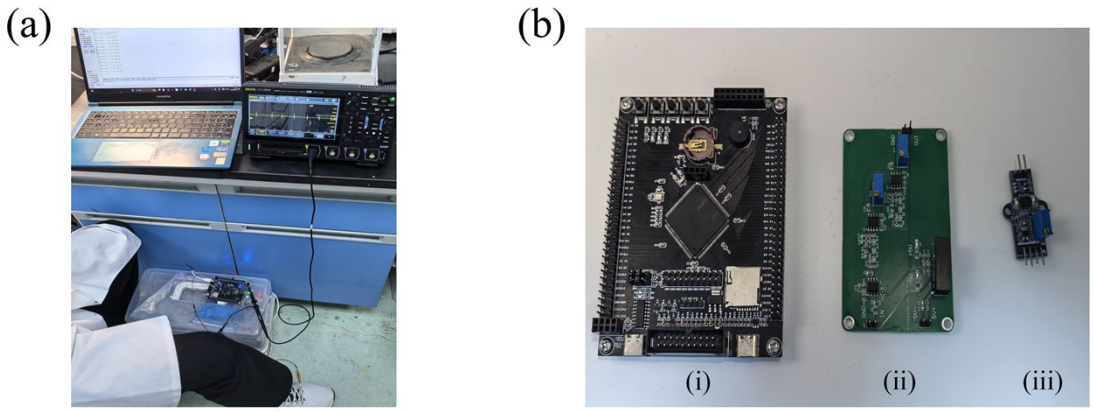

Fig. S13. Schematic and physical representation of the electronic circuit system. (a) Integration of PVDF/MXene composites with electronic circuitry, illustrating the precise correlation between piezoelectric film waveforms and real-time data acquisition. (b) PCBs of the STM32 (i), filtering circuit (ii), and charge amplification circuit (iii).

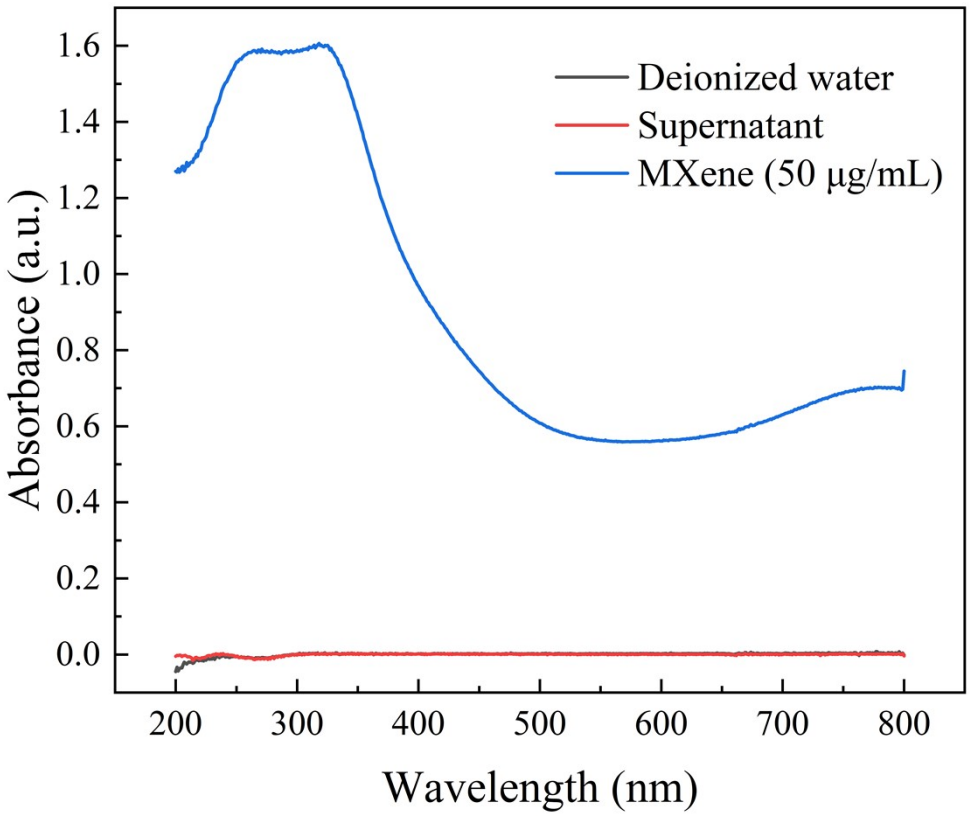

Fig. S14. Stability and leaching evaluation of the PVDF/MXene membrane. UV-vis absorption spectra of deionized water (blank), the supernatant obtained after immersing the PVDF/MXene membrane in solution for 24 h under continuous stirring, and a standard $Ti_3C_2T_x$ MXene solution (50 μg/mL).

Table S2 benchmarks piezoelectric PVDF films, MXene-based antibacterial hydrogels, piezoelectric hydrogels, and the antibacterial piezoelectric film developed in this work. On the sensing side, our PVDF/MXene film achieves a high β-phase content of 93.3% with a sensitivity of 0.502 V/N (≈ 313 mV/kPa), top-ranked among the piezoelectric films. Notably, although very high β-phase contents of PVDF film were reported (e.g., > 95%), their sensitivities are typically much lower (0.048 V/N), indicating that our film balances β-phase content and transduction efficiency more effectively.

Table S2. A summary of different piezoelectric films, antibacterial hydrogels and piezoelectric hydrogels, including component, type, β-phase content, sensitivity, response time, output voltage, NIR heating rate, and bacterial rate.

Component	Type	β-phase content	Sensitivity	Response time	Output voltage	NIR heating rate and bacterial rate	Reference
PVDF/chitosan	Piezoelectric film	63.70%	0.234 V/N	/	10.34 V (18 N)	/	2
PVDF/GO	Piezoelectric film	54.1%	0.039 V/N	/	4.93 V (120 N)	/	3
PVDF/MXene	Piezoelectric film	89.71%	0.092 V/N	/	3.15 V (24.13 N)	/	4
CS-PZ/PM	Piezoelectric film	81.50%	0.751 V/N	/	4.8 V (11 N)	/	5
PVDF/MXene	Piezoelectric film	> 95%	0.048 V/N	3.1 ms (response and recovery time)	~8 V (150 N)	/	6
PVDF/MXene	Piezoelectric film	/	0.33 V/N	/	10.05 V (30 N)	/	7
PVDF/MXene	Piezoelectric film	Enhanced	0.075 V/N	14 ms	~4.4 V (53.76 N)	/	8
PVDF/MXene	Piezoelectric film	93.4%	/	/	15.2 V (1.3 N)	/	9
CMC-Ty/MXene	Antibacterial hydrogel	/	/	/	/	2 min, ~50 °C (1 W/cm^2), > 99%	10
i-Lyso@Alg	Antibacterial hydrogel	/	/	/	/	10 min, ~48.8 °C (1 W/ cm^2), > 98%	11
CQ-HA/MXene	Antibacterial hydrogel	/	/	/	/	10 min, ~43 °C (1 W/ cm^2), > 98%	12
PAP-MCP	Piezoelectric hydrogel	/	2.88 mV/N	66 ms	1.41 V (50 N)	/	13
PAAN/Gly/Zn^{2+}	Piezoelectric hydrogel	/	0.0124 V/N	31 ms	0.06 V (19.1 N)	/	14
DNCP	Piezoelectric hydrogel	/	0.0123 V/N	86 ± 6 ms	0.125V (7.2N)	/	15
PVDF/MXene	Antibacterial piezoelectric film	93.3%	0.502 V/N	2.24 ms	7-8 V (15 N)	60 s, ~60 °C (0.3 W/ cm^2), > 99%	**This work**

On the antibacterial side, bactericidal efficacy of MXene hydrogels can reach > 98%, but they often require 1 W/cm^2 for 2-10 minutes to be heated to only ~ 43-50 °C. In contrast, our dry electrospun PVDF/MXene film delivers an antibacterial efficiency of > 99% with a rapid increase in the temperature higher than 30 °C within 60 s at just 0.3 W/cm^2. Importantly, most of the reported piezoelectric films lack antibacterial

functionality, while antibacterial hydrogels generally lack high piezoelectric output. Our PVDF/MXene membrane uniquely has integrated bifunctionalities, since it inherits the strong photothermal antibacterial capability characteristic of MXene hydrogels and the high sensitivity of MXene-containing electrospun PVDF films, providing a comprehensive platform for intelligent antibacterial materials, intelligent health-management interfaces, and wearable health-monitoring devices.

Reference

1. S. Gee, B. Johnson and A. L. Smith, *J. Membr. Sci.*, 2018, **563**, 804-812.
2. S. Y. Zhou, H. J. Zhang, C. Z. Du, M. Liu, L. M. Liu and Y. Zhang, *ACS Appl. Electron. Mater.*, 2024, **6**, 2575-2583.
3. G. Z. Chen, G. Chen, L. Pan and D. S. Chen, *Diamond Relat. Mater.*, 2022, **129**, 109358.
4. J. Zhang, T. Yang, G. Tian, B. Lan, W. Deng, L. Tang, Y. Ao, Y. Sun, W. Zeng, X. Ren, et al., *Adv. Fiber Mater.*, 2024, **6**, 133-144.
5. M. D. Zhang, Z. F. Tan, Q. L. Zhang, Y. T. Shen, X. Mao, L. Wei, R. J. Sun, F. L. Zhou and C. K. Liu, *ACS Appl. Mater. Interfaces*, 2023, **15**, 30849-30858.
6. Q. Y. Zhao, L. Yang, Y. Z. Ma, H. J. Huang, H. Y. He, H. L. Ji, Z. F. Wang and J. H. Qiu, *J. Alloys Compd.*, 2021, **886**, 161069.
7. M. Fahad, A. Waqar, D. Park and B. Kim, *J. Ind. Eng. Chem.*, 2025, **149**, 657-675.
8. L. Jin, Y. Ao, T. Xu, J. Zhang, Y. Zou, B. Lan, S. Wang, W. Deng and W. Yang, *J. Mater. Chem. A*, 2025, **13**, 14446-14454.
9. R. Han, L. Zheng, G. Li, G. Chen, S. Ma, S. Cai and Y. Li, *ACS Appl. Mater. Interfaces*, 2021, **13**, 46738-46748.
10. X. Zhou, W. Ma, J. Jiang, J. Dang, R. Lv, H. Wang, M. Ma, D. Sun and M. Zhang, *Biomater. Adv.*, 2025, **169**, 214157.
11. Z. Y. Chen, W. T. Cao, Y. T. Liu, H. B. Liu, J. Ru, M. T. Yin, X. Luo, Y. M. Zhang and F. Chen, *Int. J. Biol. Macromol.*, 2024, **279**, 135527.
12. X. B. Ma, A. A. Wang, X. L. Zhang, J. Zhang, J. W. Li, X. Fu, P. Wang, Y. T. Zhao and X. N. Huang, *Mater. Today Bio*, 2024, **29**, 101265.
13. S. Zheng, A. Liu, J. Liu, W. Wu, X. Zhou, L. Chen and K. Liu, *Nano Energy*, 2025, **133**, 110467.
14. Y. D. Shi, Y. J. Guan, M. J. Liu, X. C. Kang, Y. Tian, W. C. Deng, P. Yu, C. Y. Ning, L. Zhou, R. M. Fu, et al., *ACS Nano*, 2024, **18**, 3720-3732.
15. C. Zhang, S. H. Kwon, A. Huerta, Z. P. Jiang, M. D. Sun and L. Dong, *ACS Mater. Lett.*, 2025, **7**, 2607-2616.